Framework for Donor-Qubit Spatial Metrology in Silicon with Depths Approaching the Bulk Limit

Maxwell T. West[1] and Muhammad Usman[1,2,*]

[1]*Center for Quantum Computation and Communication Technology, School of Physics, The University of Melbourne, Parkville, Victoria 3010, Australia*
[2]*School of Computing and Information Systems, Melbourne School of Engineering, The University of Melbourne, Parkville, Victoria 3010, Australia*

Impurities in silicon are fundamental to a variety of modern nanoscale technologies working in both classical and quantum regimes of operation. The aggressive miniaturization of electronic devices has reduced their size to the nanometer scale, where the exact count and positioning of a few impurity atoms dictates their overall operation and performance. In the emerging area of quantum hardware development, single-impurity spins in silicon form excellent qubits and identifying their exact locations is important to engineer two-qubit interactions for high-fidelity quantum operations and the associated quantum control systems. This work reports a theoretical framework for the spatial metrology of single-impurity atoms in silicon with exact atomic precision for impurity depths approaching the bulk limit. The application of a carefully designed electric field pulls the impurity wave functions toward the surface, leading to spatially resolved scanning tunneling microscope images of electronic states exhibiting features that distinctly depend on the exact locations of the impurity atoms beneath the silicon surface. After verification of the developed metrology technique for individual atom positions, we train a machine-learning algorithm that can autonomously perform the metrology with high throughput in the presence of noise commensurate with experimental measurements. A future experimental implementation of the established capability for impurity-atom characterization is anticipated to play an important role in the design of a wide range of electronic and quantum devices.

I. INTRODUCTION

Silicon has been a workhorse material system of the microelectronic industry for several decades, due to its highly versatile electronic properties. The aggressive scaling of silicon devices has led to the nanoscale regime, where the size of the active region of electronic devices is approaching ≤ 10 nm scale. At this ultrasmall scale, the devices consist of only a countable number of impurity atoms, the locations and count of which are critical to their functionalities [1–3]. Along with the innovations in classical electronics, the immense progress in the field of quantum computing has ignited a race to build a fault-tolerant universal quantum computer. Of many platforms for quantum hardware design and implementation, silicon is again at the forefront, offering highly promising properties for solid-state spin qubits based on individual impurity atoms [2,4–8]. In these quantum devices working at the level of individual atoms, the exact locations of impurities play a crucial role in implementing controllable single-

and two-qubit operations with high fidelities [8,9], which are fundamental to the design of a scalable quantum computer architecture [7,10]. Consequently, the determination of exact impurity-atom locations in silicon is an important problem, with implications for nanoscale devices working in both classical and quantum regimes of operation.

This work builds upon our previous formulation of a spatial metrology technique, which has demonstrated the pinpointing of impurity atoms in silicon with exact lattice-site precision and with impurity depths up to 5 nm below the passivated silicon surface [11]. The technique is based on the low-temperature scanning tunneling microscope (STM) images of the spatial profiles of electron wave functions bound to phosphorus and arsenic impurity atoms in silicon [11,12]. It has been shown that each location of an impurity atom in the silicon crystal leads to a distinct feature map in the spatially resolved STM image of the electron wave function, which can be uniquely associated to the location of the impurity. The metrology has subsequently been shown to work with high precision for closely spaced subsurface donor pairs [13] and single dopants in strained silicon [14]. However, as the depth of the impurity

---
*musman@unimelb.edu.au

atom is increased beyond 5 nm below the passivated silicon surface, the electron-wave-function interaction with the reconstructed silicon surface becomes weak and the corresponding STM image features no longer remain distinct, signifcantly reducing the accuracy of the metrology technique (see Fig. 1). As experimental qubit devices are expected to have donor qubits placed deep inside the silicon to avoid unwanted interactions with the surface, the extension of the metrology technique is warranted to enable its working for deeper impurity positions and is addressed in this work.

This work reports the theoretical development of a metrology framework that is based on the application of a carefully designed electric field, which can enable the STM images to be employed for the pinpointing of the exact impurity-atom locations up to 10 nm below the silicon surface. We show that the donor depth of 10 nm reaches the bulk limit as the surface effects on donor electronic states become negligible (see Fig. S1 in the Supplemental Material [15]). The technique is underpinned by the fact that the measured STM images are dominated by the $d_{z^2-(1/3)r^2}$ tip orbital [11] due to the silicon-valley configuration [16] and are therefore proportional to the magnitude squared of the second derivatives of the impurity wave functions closer to the surface [17]. By investigating the spatial profile of the wave functions in the silicon crystal of impurities beyond a depth of 5 nm we find that, regardless of their exact position, by the time they have reached the surface, their second derivatives are simply decreasing almost uniformly exponentially in magnitude, without the strongly distance-dependent oscillations that render impurities close to the surface mutually distinguishable [see Fig. 2(a)].

In this work, we show that the application of an electric field pulls the electron wave function toward the surface, increasing both its amplitude and slope. This restores the distinct feature symmetry and brightness in STM images, allowing the spatial metrology to be reliably performed even when the impurity depths are reaching 10-nm range. This is evident from Fig. 1, which schematically shows the silicon crystal and a few placements of donor atoms below the reconstructed surface. The figure also plots spatially resolved STM images for each donor location without and with the application of electric fields. The STM images corresponding to the donor locations closer to the surface exhibit distinct features; however, as the donor locations become deeper, the distinction between STM features gradually fades. The application of an electric field restores the feature maps even for deep donor positions.

The working of the developed metrology technique is demonstrated by systematically placing impurity atoms at the available lattice sites in the silicon crystal at distances between 5 and 10 nm from the surface and carefully designing electric field magnitudes that can be applied at each depth to enable reliable pinpointing of impurity-atom locations. We note that electric fields of small
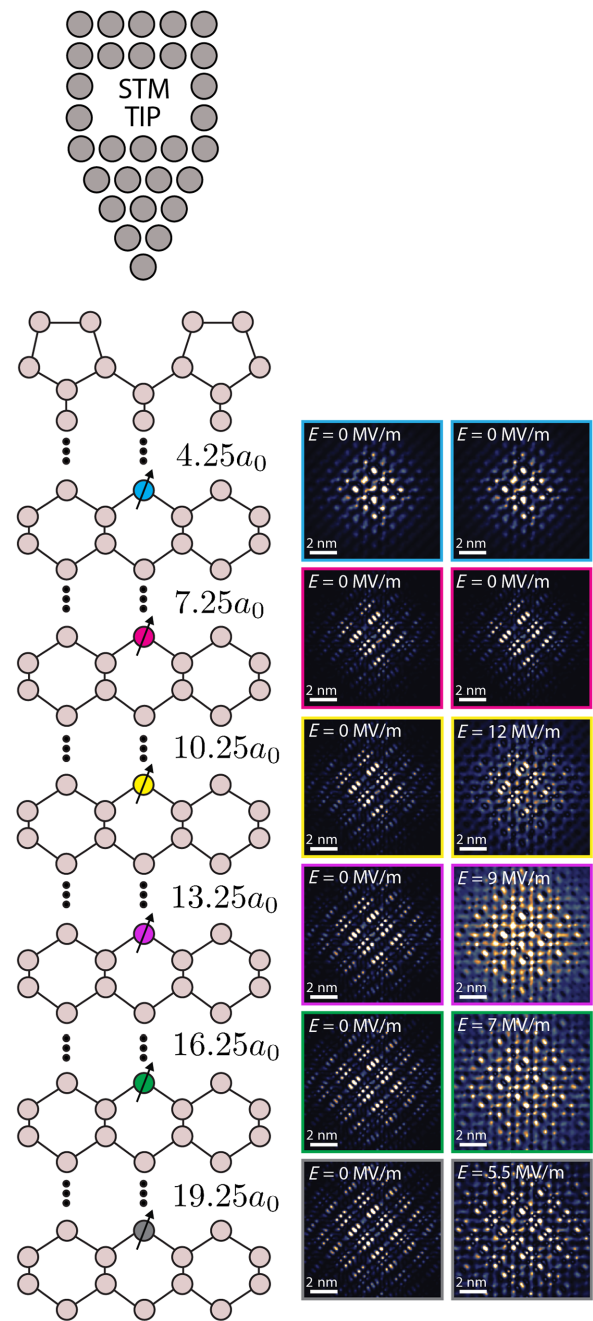
FIG. 1. STM-based metrology for the exact position of subsurface dopants in silicon. Theoretically computed STM images of phosphorus (P) donors in Si at various depths both with (right column) and without (left column) an externally applied electric field. From the zero-field images, we see that donors close to the surface produce distinguishable STM images (see, e.g., the $4.25a_0$ and $7.25a_0$ images) but beyond a depth of $10a_0$, the images become nearly indistinguishable without the help of an electric field (e.g., the $13.25a_0$ and $16.25a_0$ images).

magnitude are not sufficient to pull the wave functions enough to restore distinguishability of image features. On the contrary, electric fields of very large magnitude result
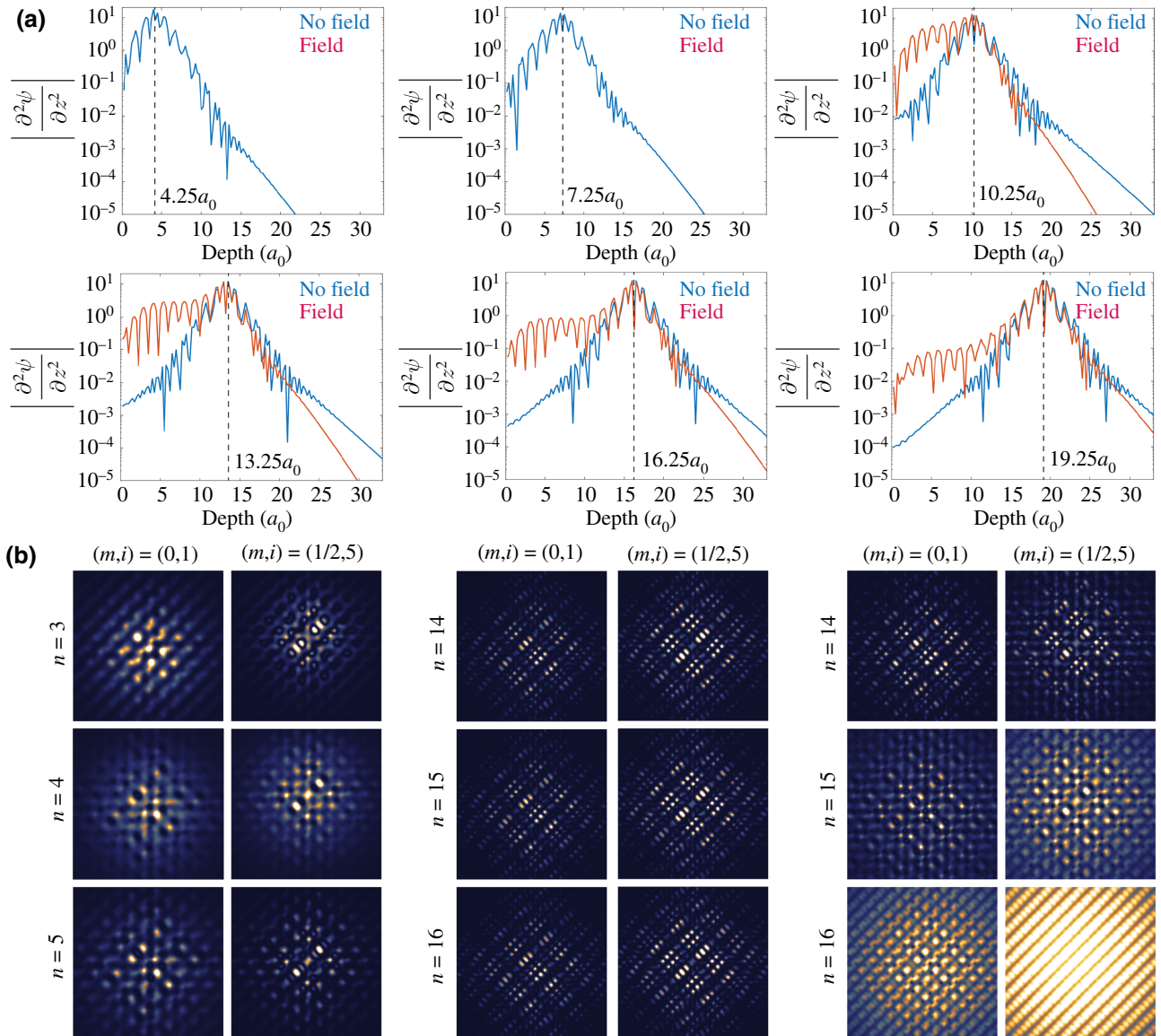
FIG. 2.   (a) The magnitude of the second derivative with respect to the depth direction of the wave functions of donors at the depths shown in Fig. 1, both with (red) and without (blue) externally applied electric fields. For shallow depths, no field is required. The electric fields turn the second derivatives of deep donor wave functions near the surface into complicated oscillatory functions, leading to distinguishable STM images, as the tunneling matrix element is proportional to $(2/3)\partial^2\psi/\partial z^2 - (1/3)(\partial^2\psi/\partial x^2 + \partial^2\psi/\partial y^2)$. (b) Shallow donors produce STM images that depend uniquely on their position $L_m^i(n)$. (c) While variation as a function of m and i continues to be observed, deep donors differing only in their value of n produce indistinguishable images. (d) The application of a well-chosen electric field renders distinguishable deep donors differing only in their value of n. Figures (b) (d) are extended to show the other possible values of (i, m) in Figs. S3 S5 in the Supplemental Material [15].

in complete ionization of the electron wave functions at the surface, leading to STM images that do not exhibit distinct feature maps. Therefore, at each depth location, the magnitude of the electric field is designed to allow optimal feature map selection. Our assumption is that the impurity-atom placement will be based on state-of-the-art STM precision fabrication techniques [2,13], which allow impurities to be placed within $\pm a_0$ uncertainty, where a_0 is the silicon lattice constant. Therefore, the impurity atoms can

only occupy possible locations inside $d \pm a_0$ when fabrication is done with target depth d. It is important to point out that the magnitude of the optimal electric field required for spatial metrology of impurities is inversely proportional to the depth of the impurity atom. For deeper impurity positions (in the range of 9–10 nm depth), which are more relevant for electronic and quantum computing devices, the magnitudes of the optimal electric fields determined by our work are in the range of 5–6 MV/m, which is

commensurate with the electric fields typically applied in STM-fabricated devices [18].

In our work, the determination of exact donor positions is based on pixel-by-pixel comparison of STM images, clearly indicating a peak corresponding to the location of the impurity. However, such a manual pixel-by-pixel comparison technique is slow and erroneous, in particular in the context of a large-scale error-protected quantum computer in which millions of qubits are required for fault-tolerant information processing [19]. To automate the metrology process and to allow its robust and fast processing, we train a machine-learning algorithm (a convolutional neural network, or CNN) based on a large number of simulated STM images, which has previously been reported to work very well with STM images for shallow impurity depths [20]. The training of the CNN allows the donor-position metrology to be performed with nearly 100% accuracy and minimal human interaction. As the fabrication of impurity atoms and measurements of STM images is an expensive task, we envision that our well-trained CNN framework will be able to work in conjunction with experimental STM setup to allow fast, reliable, and scalable metrology of impurity atoms in large-scale quantum computers and classical nanoelectronic devices.

II. THEORETICAL APPROACH

The computation of phosphorus-dopant wave functions is performed by solving an atomistic $sp^3d^5s^*$ tight-binding Hamiltonian [21] with spin-orbit coupling. The phosphorus donor atom is placed in a large silicon box consisting of roughly 3×10^6 atoms (40-nm dimension in each direction). The confusing potential on the phosphorus atom is represented by a comprehensive description of the central-cell effects, which include nonstatic dielectric screening of the donor potential [22]:

$$U(r) = \frac{-e^2}{\epsilon(0)r}$$
$$\times \left[1 + A\epsilon(0)e^{-\alpha r} + (1-A)\epsilon(0)e^{-\beta r} - e^{-\gamma r} \right], \quad (1)$$

where A, α, β, and γ are fitting constants and are numerically fitted as described in the literature [23]. Additionally, the nearest-neighbor bond lengths of Si:P are strained by approximately 1.9% in accordance with the recent density functional theory study [24]. The value of U_0 at the donor-atom site is adjusted to empirically fit the binding energies of the 1s manifold of states [25,26]. The calculation of the electron wave functions also includes the effect of 2×1 surface reconstruction, leading to the formation of dimer rows at the z=0 surface [11,27]. The impact of the surface strain due to the 2×1 reconstruction is included in the tight-binding Hamiltonian by generalization of Harrison's scaling law, where the interatomic interaction energies are

modified with the strained bond length d as $(d_0/d)^\eta$, where d_0 is the unperturbed bond length of Si lattice and η is a scaling parameter, the magnitude of which depends on the type of interaction being considered, and which is fitted to obtain hydrostatic deformation potentials [21]. The boundary conditions for the silicon box are selected as closed, with dangling bond energies shifted by a large value to avoid spurious states in the working range of energy [28]. The theoretical calculations are performed using the NEMO-3D framework [26,29].

The computation of the STM images is performed by coupling the atomistic tight-binding electronic wave-function calculation with Bardeen's tunneling current formalism [30]. The wave function is decayed in the vacuum region above the reconstructed silicon surface based on the Slater orbital real-space representation [31]. For the calculation of the tunneling current, the dominant contribution has been found to come from the $d_{z^2-(1/3)r^2}$ tip orbital, which reproduces the experimentally measured data with very high accuracy [11]. The calculation of the $d_{z^2-(1/3)r^2}$ tip-orbital-dependent STM current is computed by applying the derivative rule reported by Chen [17]:

$$I_T(r_0) \propto \left| \frac{2}{3}\frac{\partial^2 \Psi_D(r)}{\partial z^2} - \frac{1}{3}\frac{\partial^2 \Psi_D(r)}{\partial y^2} - \frac{1}{3}\frac{\partial^2 \Psi_D(r)}{\partial x^2} \right|^2_{r_0}, \quad (2)$$

where Ψ_D is the donor wave function and r_0 is the position of the STM tip.

The upper boundary of the color scale used in a given simulated STM image is proportional to the maximum tunneling current calculated in that image, i.e., the maximum value of the current is effectively normalized to 1. Therefore, identically colored pixels in different images do not necessarily represent identical values of the tunneling current but, rather, identical fractions of the peak current in the respective images; the important information in the STM images lies in the relative brightness, symmetry, and extent of the features, not in the absolute values of the current.

III. RESULTS AND DISCUSSION

A. Classification of lattice sites in silicon

In order to facilitate the description of the metrology, we begin by formulating a systematic labeling scheme for classifying the lattice sites inside the Si crystal, which follows from our earlier work [11]. Silicon crystallizes in the diamond structure, with the lattice planes perpendicular to the (001) direction being divisible into four groups. Having tessellated the crystal with conventional cubic unit cells, a given plane can either pass through the bottom of a row of unit cells or at a height of $a_0/4$, $a_0/2$, or $3a_0/4$ above the bottom of a row of cells, where $a_0 \approx 0.543$ nm is the silicon lattice constant. The P donor positions can therefore be represented by $L_m^i(n)$, where $m \in \{0, 1/4, 1/2, 3/4\}$ selects a plane group, n selects a plane within that group, and i an

atom within that plane, at a depth of $d[L_m^i(n)] = (m + n)a_0$ below the surface. Our procedure for assigning a value of i is depicted schematically in Fig. S2 in the Supplemental Material [15], including hydrogen passivation and a 2×1 surface reconstruction, resulting in the formation of Si dimer rows. Because of the surface dimer rows, the depth of a P donor is not the only factor that influences the corresponding STM image; whether it is underneath the middle of a dimer row, underneath the edge of a dimer row, or in the space between two dimer rows must also be considered.

B. Revisiting the spatial metrology of shallow dopants

Before presenting our extension to the bulk regime, we first briefly outline the metrology technique previously introduced in Ref. [11], identifying the limiting factor preventing this system from being applied to P donors placed > 5 nm from the surface and then showing how the application of a well-chosen electric field can overcome this difficulty. The key observation in Ref. [11] is that donors implanted close to the surface produce unique STM images and so, having theoretically calculated a complete library of STM images corresponding to donors at all possible positions, one can deduce the exact location $L_m^i(n)$ of an experimentally implanted donor by measuring an STM image and then comparing it with the images in the library. The comparison proceeds in two key stages as developed in Ref. [11]. For completeness, we describe the procedure here, with reference to a set of sample images computed at various shallow depths, shown partially in Fig. 2(b). The full set is shown in Fig. S3 in the Supplemental Material [15].

In the first stage, the values of m and i are determined by a qualitative analysis of the image. Inspecting the two images in any given row of Fig. 2(b) (corresponding to the same value of n but different values of m and i), we observe that they have different symmetries with respect to the [110] and [−110] directions; the images with $(m, i) = (0, 1)$ are asymmetric with respect to reflections about the [110] diagonal, while those with $(m, i) = (1/2, 5)$ are symmetric. The full set of possible symmetries are displayed in Fig. S3 in the Supplemental Material [15]; in general, for a given a value of n, it has been shown in Ref. [11] that an image may be uniquely classified according to the following combination of factors: how many lobes of features it has along the [−110] direction; whether or not it has features along the [110] diagonal and whether or not it is symmetric about the [110] diagonal. For example, an image that possesses two lobes of features along the [−110] direction, no features along the [110] diagonal, and is symmetric about the [110] diagonal receives the classification $m = 1/2, i = 6$.

Having now found the values of m and i, in the second stage of the metrology the value of n is determined.

Donor positions differing only in their value of n produce images possessing the same symmetries and so the determination of n for a given experimental image proceeds by a pixel-by-pixel comparison with all theoretically computed images with the determined values of m and i. Referring again to Fig. 2(b), then (or Fig. S3 in the Supplemental Material [15]), in the first stage the correct column of the image is determined by qualitative analysis of its symmetry features and in the second stage the row is determined by a quantitative comparison with all images in that column.

C. Applicability of spatial metrology to deep dopants

While the procedure described above has been successfully used in Ref. [11] to identify donors within 5 nm of the reconstructed surface, the question of whether the method would continue to work for donors buried deep within the crystal has been left open. By inspection of the STM images of deep donors presented in Fig. 2(c) (for more values of m and i, see Fig. S4 in the Supplemental Material [15]), we observe that the first stage of the metrology continues to be successful as the various symmetries (or asymmetries) are still clearly present, which allows unique identification of i and m based on an STM image. The second stage fails, however, as can be seen by observing the extreme similarities between images in the same column and therefore differing only in their value of n. The extent of these similarities is sufficient to render the images indistinguishable in the presence of the levels of noise that would unavoidably be present in an experimental setting and so the previously published metrology [11] cannot be immediately extended to the case of deeper donors. Although the impurity wave functions oscillate in a complicated fashion close to the impurity, donors situated deep beneath the surface have wave functions that are simply exponentially decaying by the time they reach the surface [see Fig. 2(a), blue plots]. Being a surface-based technique, STM has access only to this uninformative region and it is therefore unsurprising that it struggles to distinguish between deep donors displaced by $\pm a_0$.

D. Design and application of electric fields

To enable the spatial metrology of deep donor positions (unique determination of n), we apply a constant uniform external electric field $\mathbf{E} = E\mathbf{z}$, which introduces a depth-dependent perturbation to the Hamiltonian of a donor at depth d of magnitude $U = eEd = eE(n + m)a_0$, breaking the indistinguishability between donors at $L_m^i(n)$ and $L_m^i(n \pm 1)$. The field attracts the electrons toward the surface, amplifying the small differences between the various deep donors [see Fig. 2(a), red plots]. The resulting STM images in the case $n = 15 \pm 1$ are shown in Fig. 2(d) [for more values of (m, i), see Fig. S5 in the Supplemental Material [15]] in the presence of an electric field of

magnitude 7.5 MV/m. These same positions are imaged in Fig. 2(c) (see also Fig. S4 in the Supplemental Material [15]), where the indistinguishability of donors displaced by $\pm a_0$ is observed. In the presence of this electric field, however, such images are evidently rendered distinguishable. We note that, as an unintended consequence, the images of donors with depths of $16.5a_0$ and $16.75a_0$ have now become indistinguishable (Fig. S5 in the Supplemental Material [15]), as in both of these cases the donor electron has been ionized. Given that they were previously distinguishable (without the electric field), however, this problem can be resolved by measuring STM images both with and without the applied electric field. The values of m and i can be found from the image measured without an electric field and the value of n from the image measured in the presence of the electric field.

To get a rough order-of-magnitude estimate of the field strength required to have a significant effect on the STM images, we set the resultant electric potential energy to the ionization energy of a P donor in Si, 45 meV [25]. For a donor at, say, $10a_0$, this gives a field of magnitude $E = 45$ mV/$10a_0 \sim 10$ MV/m. We therefore expect that the application of electric fields significantly weaker than 10 MV/m will not have much of an effect on the STM images of a donor at $10a_0$ and that electric fields much stronger than 10 MV/m will cause the donor electron to ionize at the surface. This is illustrated in Fig. 3 for the case $m = 1/4$, $i = 3$ (the other cases are shown in Figs. S6 S10 in the Supplemental Material [15]). The direct proportionality between depth and energy for a given electric field strength suggests that the field strength must be chosen with the target depth in mind. If we are trying to distinguish between donors at depths of $17.25a_0$,

$18.25a_0$, and $19.25a_0$, for example, the 10 MV/m field discussed above in the context of a donor at $10a_0$ would be of little help, as in all cases the donor would be ionized and its electron completely removed from the donor atom, carrying no information about the location of its parent nucleus (beyond setting a lower bound on the depth of that nucleus). For a given target depth, we must therefore find a middle ground between fields that are too weak to make an appreciable difference to the STM images and fields that are so strong that they simply ionize all of the donors in which we are interested. Our investigations suggest that this balance is best struck by choosing a field that is slightly weaker (by approximately 1 MV/m) than the field that would ionize a donor at the target depth (see Fig. 3).

E. Quantitative pixel-by-pixel comparison

We now make a quantitative estimate of our proposed metrology technique, explaining how the optimal electric field strength is determined and demonstrating its robustness to reasonable levels of arbitrary noise. We see that the inapplicability of the previous metrology [11] to deeper donors is due to the similarity of images corresponding to donors displaced by $\pm a_0$ in the depth direction. For example, direct pixel-by-pixel comparisons of deep donors at $L_{1/4}^3(19)$ and $L_{1/4}^3(19 \pm 1)$ yield $> 98\%$ similarities (Fig. 4, top right-hand corner), where, as in Ref. [11], we define a measure of similarity:

$$C(I,J) = \max\left\{0, 1 - \left[\frac{\sum_{x,y}^{N_x,N_y}|I(x,y) - J(x,y)|}{\sum_{x,y}^{N_x,N_y}I(x,y)}\right]\right\} \tag{3}$$
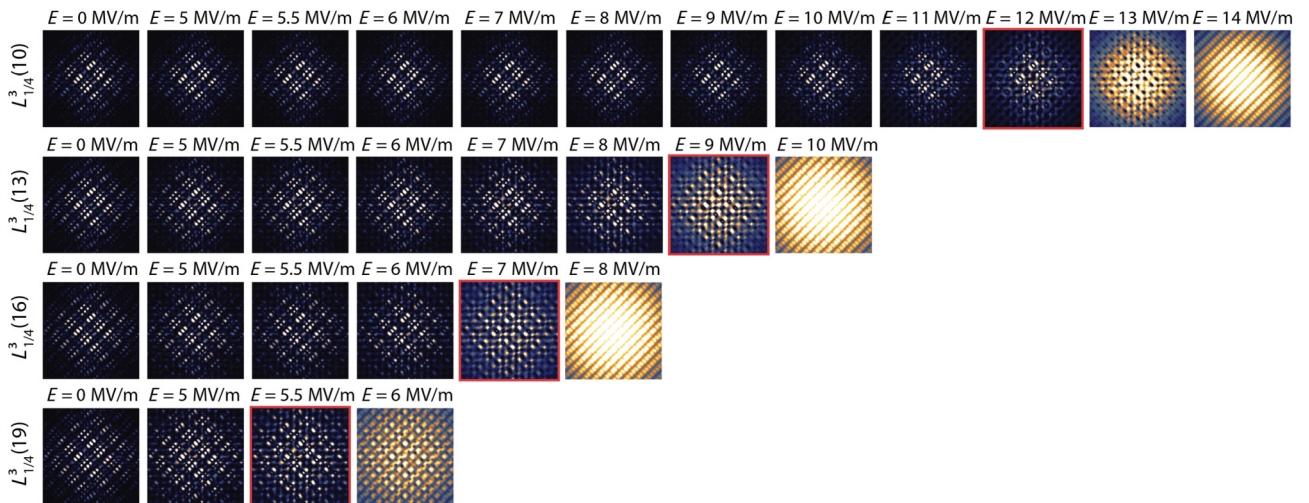
FIG. 3. STM images as a function of the depth and the electric field. The field required to optimally distinguish between images of donors at $L_m^i(n \pm 1)$ varies with n. As the electric potential experienced by the donor is proportional to its depth, small fields quickly ionize deep donors, while barely affecting more shallow donors. The image corresponding to the optimal field for the given depth range is highlighted in red. This figure shows images with $m = 1/4, i = 3$, with the other cases available in the Supplemental Material [15].
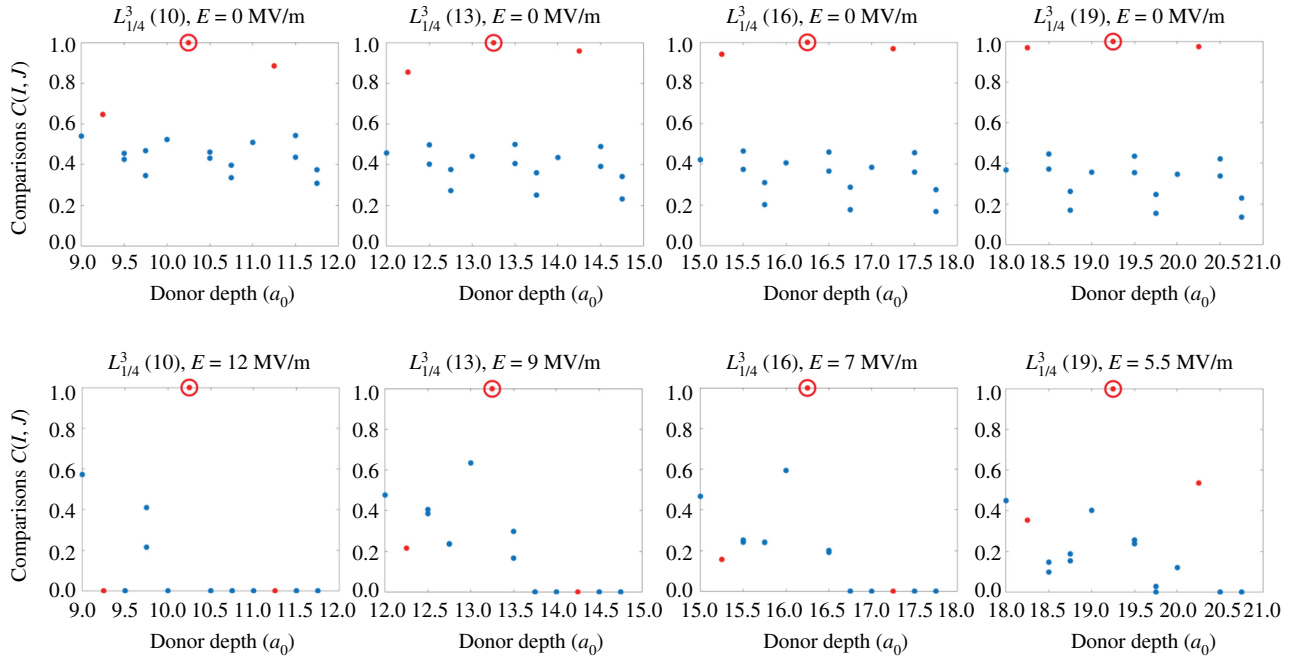
FIG. 4.   A pixel-by-pixel comparison of STM images. Direct comparison of the image I at a target depth (circled) with the images of nearby depths J [see Eq. (3)]. The blue dots correspond to locations that can be rejected by symmetry considerations. Unique identification is impractical without an applied field due to the very high (rising to $> 98\%$ by $n = 19$) comparison values but becomes possible in the presence of an applied field. These plots demonstrate the necessity of the electric field in the case $m = 1/4, i = 3$; similar plots for other values of m and i may be found in the Supplemental Material [15].

between two STM images I and J, which is 1.0 when the two images are identical and 0 when they are completely dissimilar. The values $I(x, y)$ represent the pixels of image I. The similarity values of approximately 0.98 seen in Fig. 4 indicate that for such deep donors, the metrology of Ref. [11] will fail in the presence of even a small amount of noise (blurring or asymmetrical brightness), which is unavoidable under realistic experimental conditions [11].

The situation is illustrated in the top row of Fig. 4, where the comparison values $C[L^i_m(n), L^{i'}_{m'}(n')]$ are plotted for several example sites $L^i_m(n)$ (circled) and the 17 other sites $L^{i'}_{m'}(n')$ with $n' \in \{n-1, n, n+1\}$. Of these, 15 can be distinguished by the qualitative-feature analysis described above (the blue dots), while two, corresponding to $L^i_m(n \pm 1)$ (the red dots), cannot. If the pixel-comparison values [Eq. (3)] for these two images are low, then the metrology is expected to be successful, even in the presence of some random noise. For values of $n \lesssim 10$, these values are indeed low (i.e., the images are sufficiently dissimilar) and the procedure of reading off m and i by symmetry and determining n by pixel-by-pixel comparisons has been successfully demonstrated in Ref. [11]. For $n > 10$, however, the unacceptably high values of $C[L^i_m(n), L^i_m(n \pm 1)]$ necessitate a different approach to the determination of n beyond a simple pixel-by-pixel comparison with precomputed theoretical STM images; hence our introduction of an electric field. Similar pixel-by-pixel

comparisons computed for other positioning of donors in silicon are plotted in Figs. S11–S15 in the Supplemental Material [15].

Given a target depth n, the optimal electric field magnitude is found by calculating the STM images of all donors in the groups n or $n \pm 1$ in the presence of many different fields and picking the field that minimizes the pixel-comparison value of the most similar pair of images with the same values of m and i, i.e., the "worst-case similarity" $S(n, f)$, where

$$S(n, f) = \max_{i, m} C\left[L^i_m(n, f), L^i_m(n \pm 1, f)\right], \quad (4)$$

in which $L^i_m(n, f)$ denotes the STM image of a donor at $L^i_m(n)$ in the presence of the field f. For a given depth n, then, the optimal field f_{optimal} satisfies

$$f_{\text{optimal}} = \arg\min_f S(n, f). \quad (5)$$

The lower $S(n, f_{\text{optimal}})$ is for a given n, the more easily we can distinguish between STM images around that target depth. If $S(n, f) \approx 1$, then unique classification is impossible with the field f, as two of the resultant images are almost the same. We see from the very high values of $S(n, 0)$ in Table I the necessity of applying a nonzero field and from the lower values of $S(n, f_{\text{optimal}})$ the resilience of

TABLE I. The worst-case pixel-comparison values $S(n,f)$ for various target depths n, both without a field, $S(n,0)$, and in the presence of the optimal field, $S(n,f_{\text{optimal}})$. The high values of $S(n,0)$ are indicative of the failure of the STM metrology in the absence of an applied electric field.

Target depth (a_0)	Optimal field (MV/m)	$S(n,0)$	$S(n,f_{\text{optimal}})$
10	12	0.95	0.65
11	10	0.95	0.76
12	9	0.96	0.80
13	9	0.96	0.70
14	8	0.97	0.66
15	7.5	0.97	0.57
16	7	0.97	0.83
17	6.5	0.98	0.76
18	6	0.98	0.62
19	5.5	0.98	0.87

our technique to the effect of random noise. The technique can, in principle, be extended to donors deeper than $20a_0$, limited by the precision with which the magnitude of the electric field can be controlled; increasingly precise control is needed for deeper donors. This is due to the difference between a field that has a negligible effect upon a donor and a field that ionizes it going like $1/d$, as the potential energy term added to the Hamiltonian by the electric field is proportional to the depth of the donor. While, due to computational limitations, we only consider fields that are integer or half-integer multiples of 1 MV/m, for target depths beyond $20a_0$, a finer resolution would in general be required to find an electric field that could discriminate between adjacent donors with high accuracy. Indeed, the beginning of this problem can already be seen in Table I at the target depth of $19a_0 \approx 10.3$ nm, where half-integer multiples of 1 MV/m can only reduce $S(19,f)$ to 0.87. However, donors located at a target depth of 10 nm already experience negligible surface effects and therefore metrology of donors with depths up to 10 nm is sufficient for all practical devices.

F. Machine-learning framework

The metrology described thus far is expected to work well based on pixel-by-pixel comparison at individual qubit level but one of its primary applications to a Si-P based full-scale error-protected quantum computer will likely require the identification of many millions of P donors and therefore it is desirable to develop a versatile and scalable approach that continues to perform accurately in the presence of reasonable levels of experimental noise. Machine learning is a powerful tool for image recognition and has been successfully used for the autonomous spatial metrology of shallow P donor qubits in Si [20]. We show here that, with minor modification, the previous machine-learning-based metrology can be combined with the electric field technique explored in the previous sections of this work to determine the positions of deeper donors, up to depths of $20a_0$, and in the presence of levels of noise commensurate with that of experimental reports.

The previous two-step procedure to identify the position $L_m^i(n)$ of a P donor was as follows: first, determine the values of m and i by examining the symmetry properties of the images without an applied electric field; second, determine the value of n by applying an electric field and performing a direct pixel-by-pixel comparison with the theoretically computed images of $L_m^i(n)$ and $L_m^i(n \pm 1)$. In particular, we note that images both with and without an electric field are required to uniquely determine the donor position. This is illustrated in Figs. S4 and S5 in the Supplemental Material [15]. In Fig. S4, images belonging to different columns are clearly distinguishable but those in the same column are very similar, whereas in Fig. S5, those belonging to different rows are clearly distinguishable but those in the same row are sometimes very similar, as the symmetry features are not necessarily visible in the presence of a strong field. Only with access to the images produced by the donor wave function both with and without an electric field can one uniquely identify both the row and the column based on this procedure. We would therefore not expect a machine-learning algorithm to be able to determine the exact position given solely the images with or without an electric field. This problem can be solved by merging the images from the two cases (with and without an electric field) into the training data of a neural network under the principle of supervised learning (Fig. 5). Having done this, the network now has access to all of the information that is needed to successfully identify the images in the pixel-by-pixel formulation. As in the previous sections, we restrict our focus to distinguishing images of the form $L_m^i(n), L_{m'}^{i'}(n')$ with $n' \in \{n, n \pm 1\}$. As the neural network is being given images comprised of STM images both with and without fields, however, unlike in previous sections we do not need to do any symmetry-based preprocessing to reduce the problem to distinguishing between the $3 \times 1 = 3$ images corresponding to some *given* values of m and i but, rather, we can require the network to be able to classify an image as belonging to any one of the $3 \times 6 = 18$ possible classes corresponding to any values of n', m', and i'.

A CNN is trained for each value of n. In practice, quantum computer architecture will be fabricated with only one target positioning of qubits; therefore, only one well-trained CNN will be required to perform metrology. CNNs are used due to their suitability for performing image recognition with high accuracy and efficieny. The CNNs are implemented using KERAS [32], with TensorFlow [33] as the underlying platform. In order to train (and test) a CNN, a large data set of images is required. To create this data set, we artificially apply random noise to the ideal theoretical images corresponding to each of the 18
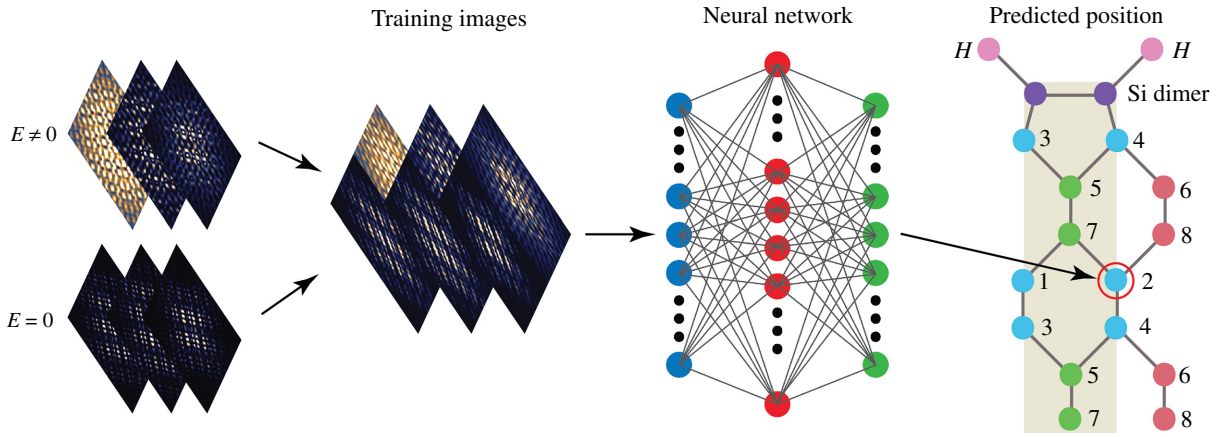
FIG. 5. The machine-learning procedure. STM images for a given position $L_m^i(n)$ are calculated both with and without the optimal field $f_{optimal}$ and are merged into a single image before being inputted into the neural network. Each network is trained on 18 000 (planar) noisy images and then tested on a further 18 000 previously unseen images that have been subjected to both planar and blurring noise.

possible donor positions resulting from a target value of n. As in a previous study [20], two distinct types of noise are considered: Gaussian blurring noise (σ_b) and planar noise (σ_p). The planar noise is generated by

$$I_{noise}(x, y) = I_{ideal}(x, y) \times N(x, y),$$

where I_{ideal} is the theoretically calculated ideal image and N is given by

$$N(x, y) = 1 + \sigma_p \left[1 + \cos(\theta)(x - x_0) + \sin(\theta)(y - y_0)\right],$$

where σ_p is a parameter that controls the magnitude of the noise, (x_0, y_0) is the donor position, and θ is selected at random each time a noisy image is generated. The noise creates an asymmetry in the ideal images, brightening one side and darkening the other (see Fig. S16 in the Supplemental Material [15]). In Gaussian blurring noise, on the other hand, the image is convolved with a Gaussian kernel,

$$K = \frac{1}{N} \exp\left\{-\frac{x^2 + y^2}{2\sigma_b}\right\},$$

where x and y are the horizontal and vertical displacements of the pixel from the center of the kernel, σ_b is a parameter that controls the magnitude of the noise, and N is a normalization factor. Examples of the application of this type of noise are shown in Figs. S16 and S17 in the Supplemental Material [15].

For each target depth, 18 000 planar noisy images are generated, 1000 for each possible donor position, with σ_p varying from 0.015 to 0.15 in increments of 0.015. The network is trained on these images for two epochs, with 1000 steps per epoch. In the testing phase, Gaussian blurring noise is introduced alongside the planar noise, with the blurring parameter σ_b varied from 2.5 to 7 in increments of 0.5. As in the training phase, 1000 noisy images

are generated for each possible donor position for testing. At the upper levels of the noise parameters, the combination of blurring and planar noise is quite significant and the success of the metrology in this regime demonstrates the robustness of the technique. The accuracy achieved by the neural networks for each target depth in identifying the test images is shown in Table II. The final CNN suffers a slight reduction in accuracy (approximately 95%), which is consistent with the results of the previous section, based on pixel-by-pixel comparison, where it is found that $S(19, f_{optimal}) = 0.87$, far higher than for any other value of n and therefore indicative of a set of images more difficult to distinguish between in the presence of noise. Nevertheless, the machine-learning framework demonstrates excellent accuracy to perform spatial metrology for all the possible locations up to about 10 nm depth from the silicon surface.

G. Implementation of applied electric fields

The formulated spatial metrology technique for deep donor positions is based on the application of an external

TABLE II. The accuracy achieved by the CNNs on the unseen test data for their respective values of n.

Target depth (a_0)	Accuracy achieved (%)
10	99.98
11	100
12	99.42
13	100
14	100
15	100
16	99.97
17	99.86
18	99.93
19	95.54

electric field that allows unique determination of donor depths. We note that for donor depths approaching the bulk limit (9–10 nm), the magnitude of electric field required is around 5–6 MV/m, which is commensurate with the applied electric fields reported in the literature [18,34]. In practice, such electric fields may be applied to the donor system in several different ways; for example, by applying a voltage to metallic gates fabricated on an insulating SiO_2 layer atop the silicon surface [4], by fabricating STM patterned gates buried inside the silicon [7], or by applying through the STM tip itself [34]. A recent study has reported that a similar impact of electric field arises from both top gates and buried STM-patterned gates [35], when used to tune the two qubit interactions, which is also the case in our work. We also note that for the design of a large-scale quantum computer architecture, the qubit control requires gates to be fabricated directly above and below the donor qubit plane [10].

For the purpose of carrying out the spatial metrology described in this work, however, the gates above the donor qubit plane must be sufficiently far apart to allow STM measurements of wave-function images, while inducing a reasonably uniform electric field to preserve the STM image symmetries. We analyze the construction of such a split top gate, which is divided into two gates placed symmetrically above the donor qubits, the combined impact of which will be an approximately uniform and vertical electric field in the region of interest (see Fig. S18 in the Supplemental Material [15]). In order to verify that such a configuration would yield similar STM images to those discussed earlier under the assumption of a uniform electric field $\mathbf{E} = E\mathbf{z}$, the potential landscape resulting from two such gates (separated by 8 nm in our simulation) is simulated using the COMSOL software package [36]. This potential is then a direct input to the tight-binding Hamiltonian and a series of test images are simulated (see Fig. S18 in the Supplemental Material [15]). The strong similarities between the images calculated in the ideal case and those calculated using the gate-induced potential give confidence that the metrology will be robust to imperfections in the applied electric field induced by such experimental design constraints. Indeed, when computed STM images from the split gate design are present in the test data of the trained machine-learning framework, the metrology is successful with very high accuracy. We also note that an alternative method for the application of an external electric field may be through the STM tip bias, which has previously been reported for shallow donor configurations [34]. Such tip-induced fields result in a quantum dot closer to the silicon surface that interacts with the donor electron, leading to quasiparticle STM images. Even at large electric fields (of the order of 13 MV/m) and shallow donor depths, the quasiparticle images retain many of the zero-field image features that are expected for shallow depths. For deep donor depths such as investigated in this work,

it is anticipated that the STM image under electric fields in the range of 5–6 MV/m should experience relatively smaller perturbation and that the well-trained machine-learning algorithm should be able to perform metrology with high precision, as demonstrated in this work in the presence of fairly large noise perturbations.

IV. CONCLUSIONS

In this work, we propose an STM-based spatial metrology for P donor qubits in Si, enabling the pinpointing of the exact locations of atomic spin qubits at depths of up to 10 nm below the reconstructed silicon surface, twice the previously supported depth, and in a regime where the donors exhibit bulklike behavior. The metrology is based on the idea of applying an external electric field of carefully designed magnitude, which partially attracts the impurity-bound electron wave function toward the reconstructed silicon surface, to be directly scanned by the STM. A direct pixel-by-pixel comparison of the computed STM images of the electron wave functions indicates unique image features, which can be attributed to the exact donor position in the silicon lattice. We also train and apply a machine-learning algorithm that offers the potential for robust, autonomous, and fast implementation of the metrology technique, which will be important in the context of large-scale error-corrected quantum computer architecture. Our work may constitute a valuable step forward for applications of the Si:P system in quantum electronic and computing devices where the P donors are required to be buried deep within the crystal, so as to shield them from surface effects and therefore experience the pure environment of bulk silicon, and the associated long spin coherence times.

The data that support the findings of this study are available within the paper and its Supplemental Material [15]. The accompanying Supplemental Material [15] consists of 18 supplementary figures that provide additional data to support the findings of the main paper.

[1] M. Pierre, R. Wacquez, X. Jehl, M. Sanquer, M. Vinet, and O. Cueto, Single-donor ionization energies in a nanoscale CMOS channel, Nat. Nanotechnol. **5**, 133 (2010).

[2] M. Fuechsle, J. A. Miwa, S. Mahapatra, H. Ryu, S. Lee, O. Warschkow, L. C. L. Hollenberg, G. Klimeck, and M. Y. Simmons, A single-atom transistor, Nat. Nanotechnol. **7**, 242 (2012).

[3] A. Ionescu and H. Riel, Tunnel field-effect transistors as energy-efficient electronic switches, Nature **479**, 329 (2011).

[4] B. E. Kane, A silicon-based nuclear spin quantum computer, Nature **393**, 133 (1998).

[5] J. Pla, K. Y. Tan, J. P. Dehollain, W. H. Lim, J. J. L. Morton, F. A. Zwanenburg, D. N. Jamieson, A. S. Dzurak, and A. Morello, High-fidelity readout and control of a nuclear spin qubit in silicon, Nature **496**, 334 (2013).

[6] A. Tyryshkin, S. Tojo, J. Morton, H. Riemann, N. Abrosimov, P. Becker, H. Pohl, T. Schenkel, M. Thewalt, K. Itoh, and S. Lyon, Electron spin coherence exceeding seconds in high-purity silicon, Nat. Mater. **11**, 143 (2012).

[7] C. D. Hill, E. Peretz, S. Hile, M. House, M. Fuechsle, S. Rogge, M. Y. Simmons, and L. Hollenberg, A surface code quantum computer in silicon, Sci. Adv. **1**, e1500707 (2015).

[8] M. Usman, Recent progress in atomistic modelling and simulations of donor spin qubits in silicon, Comput. Mater. Sci. **193**, 110280 (2021).

[9] M. J. Testolin, C. Hill, C. J. Wellard, and L. C. L. Hollenberg, Robust controlled-NOT gate in the presence of large fabrication-induced variations of the exchange interaction strength, Phys. Rev. A **76**, 012302 (2007).

[10] C. Hill, M. Usman, and L. Hollenberg, An exchange-based surface-code quantum computer architecture in silicon (2021), ArXiv:2107.11981.

[11] M. Usman, J. Bocquel, J. Sal, B. Voisin, A. Tankasala, R. Rahman, M. Y. Simmons, S. Rogge, and L. Hollenberg, Spatial metrology of dopants in silicon with exact lattice site precision, Nat. Nanotechnol. **11**, 763 (2016).

[12] J. Sal, J. A. Mol, R. Rahman, G. Klimeck, M. Y. Simmons, L. C. L. Hollenberg, and S. Rogge, Spatially resolving valley quantum interference of a donor in silicon, Nat. Mater. **13**, 605 (2014).

[13] B. Voisin, J. Bocquel, A. Tankasala, M. Usman, J. Sal, R. Rahman, M. Y. Simmons, L. Hollenberg, and S. Rogge, Valley interference and spin exchange at the atomic scale in silicon, Nat. Commun. **11**, 6124 (2020).

[14] B. Voisin, K. Ng, J. Sal, M. Usman, J. Wong, A. Tankasala, B. Johnson, J. McCallum, L. Hutin, B. Bertrand, M. Vinet, N. Valanoor, M. Simmons, R. Rahman, L. Hollenberg, and S. Rogge, Valley population of donor states in highly strained silicon, Nov. (2021), ArXiv:2109.08540.

[15] See the Supplemental Material at http://link.aps.org/supplemental/10.1103/PhysRevApplied.17.024070 for Figs. S1 S18.

[16] M. West and M. Usman, Influence of sample momentum space features on scanning tunnelling microscope measurements, Nanoscale **13**, 16070 (2021).

[17] C. J. Chen, Tunneling matrix elements in three-dimensional space: The derivative rule and the sum rule, Phys. Rev. B, **42**, 8841 (1990-I).

[18] S. Hile, L. Fricke, M. G. House, E. Peretz, C. Y. Chen, Y. Wang, M. Broome, S. K. Gorman, J. G. Keizer, R. Rahman, and M. Y. Simmons, Addressable electron spin resonance using donors and donor molecules in silicon, Sci. Adv. **4**, 1459 (2018).

[19] S. Gicev, L. C. L. Hollenberg, and M. Usman, A scalable and fast artificial neural network syndrome decoder for surface codes (2021), ArXiv:2110.05854.

[20] M. Usman, Y. Wong, C. Hill, and L. Hollenberg, Framework for atomic-level characterisation of quantum computer arrays by machine learning, npj Comput. Mater. **6**, 19 (2020).

[21] T. B. Boykin, G. Klimeck, and F. Oyafuso, Valence band effective-mass expressions in the $sp^3d^5s^*$ empirical tight-binding model applied to a Si and Ge parametrization, Phys. Rev. B **69**, 115201 (2004).

[22] M. Usman, R. Rahman, J. Sal, J. Bocquel, B. Voisin, S. Rogge, G. Klimeck, and L. C. L. Hollenberg, Donor hyperfine Stark shift and the role of central-cell corrections in tight-binding theory, J. Phys.: Cond. Matt. **27**, 154207 (2015).

[23] H. Nara, Screened impurity potential in Si, J. Phys. Soc. Jpn. **20**, 778 (1965).

[24] H. Overhof and U. Gerstmann, *Ab initio* Calculation of Hyperfine and Superhyperfine Interactions for Shallow Donors in Semiconductors, Phys. Rev. Lett. **92**, 087602 (2004).

[25] M. Usman, C. D. Hill, R. Rahman, G. Klimeck, M. Y. Simmons, S. Rogge, and L. C. L. Hollenberg, Strain and electric field control of hyperfine interactions for donor spin qubits in silicon, Phys. Rev. B **91**, 245209 (2015).

[26] S. Ahmed, N. Kharche, R. Rahman, M. Usman, S. Lee, H. Ryu, H. Bae, S. Clark, B. Haley, M. Naumov, F. Saied, M. Korkusinski, R. Kennel, M. McLennan, T. B. Boykin, and G. Klimeck, Multimillion Atom Simulations with NEMO 3-D, *Springer Encyclopedia of Complexity and Systems Science (Berlin: Springer)*, 5745, 2009.

[27] B. I. Craig and P. V. Smith, The structure of the Si(100)2 × 1 : H surface, Surf. Sci. **226**, L55 (1990).

[28] S. Lee, F. Oyafuso, P. von Allmen, and G. Klimeck, Boundary conditions for the electronic structure of finite-extent embedded semiconductor nanostructures, Phys. Rev. B **69**, 045316 (2004).

[29] G. Klimeck, S. Ahmed, N. Kharche, M. Korkusinski, M. Usman, M. Parada, and T. Boykin, Atomistic simulation of realistically sized nanodevices using NEMO-3D Part II: Applications, IEEE Trans. Elect. Dev. **54**, 2090 (2007).

[30] J. Bardeen, Tunnelling from a Many-Particle Point of View, Phys. Rev. Lett. **6**, 57 (1961).

[31] J. C. Slater and G. F. Koster, Simplified LCAO method for the periodic potential problem, Phys. Rev. **94**, 1498 (1954).

[32] F. Chollet, KERAS. https://github.com/fchollet/keras, 2015.

[33] M. Abadi, *et al.*, TensorFlow: Large-scale machine learning on heterogeneous systems, 2015. Software available from https://www.tensor ow.org/.

[34] J. Sal, B. Voisin, A. Tankasala, J. Bocquel, M. Usman, M. Simmons, L. Hollenberg, R. Rahman, and S. Rogge, Valley Filtering in Spatial Maps of Coupling between Silicon Donors and Quantum Dots, Phys. Rev. X **8**, 031049 (2018).

[35] Y. Wang, A. Tankasala, L. Hollenberg, G. Klimeck, M. Y. Simmons, and R. Rahman, Highly tunable exchange in donor qubits in silicon, NPJ Quantum Inf. **2**, 16008 (2016).

[36] COMSOL MULTIPHYSICS® v. 5.6. www.comsol.com. COMSOL AB, Stockholm, Sweden.